International Journal of Mechanical Sciences 161–162 (2019) 105025

Contents lists available at ScienceDirect

International Journal of Mechanical Sciences

journal homepage: www.elsevier.com/locate/ijmecsci

Novel mechanical behaviors of DNA-inspired helical structures with chirality

Bowen Zheng[a,b], Yilun Liu[c], Jingran Liu[c], Sha Yin[a,b,c], Jun Xu[a,b,*]

[a] Department of Automotive Engineering, School of Transportation Science and Engineering, Beihang University, Beijing, 100191, China,
[b] Vehicle Energy & Safety Laboratory (VESL), Beihang University, Beijing, 100191, China,
[c] State Key Laboratory for Strength and Vibration of Mechanical Structures, School of Aerospace Engineering, Xi'an Jiaotong University, Xi'an, 710049, China,

ARTICLE INFO

Keywords:
DNA-inspired structure
Chirality
Theoretical model
Finite element analysis
Deformation mode

ABSTRACT

Artificially designed structures with chirality are able to possess novel mechanical properties, for example, chiral honeycombs with negative Poisson's ratio and chiral acoustic metamaterials. Inspired by the chiral nature of double-helical structure of DNA molecule, in this paper, we present a design of helical structure with chirality and study its mechanical behaviors through experimental characterization, theoretical analysis and numerical simulation. A compression-twisting coupling deformation mode is observed for different types of DNA-inspired helical structures due to the competition among compression, bending and twisting energy of the helical structures and tension energy of the interlinks. We find that interlinks between two intertwined helices are decisive to the compression-twisting coupling deformation mode and both chiral and non-chiral behaviors of the structures can be quantitively captured by our established theoretical and numerical models. The influences of various geometric parameters on the stiffness and deformation mode are discussed. Finally, we present two types of superposed structures that behave differently, showing a high designability of the DNA-inspired structures. This study exploits the chirality of bio-inspired structures and uses it in structural design with novel mechanical properties, which may shed light on the development of bio-inspired mechanical metamaterials, impact energy absorbers, multi-functional composite materials and among others.

1. Introduction

Chirality, an important concept in many branches of science, refers to the property of non-superposability to the mirror image [8]. Objects with chirality exist from nanoscale to macroscale, to exemplify, carbon nanotubes [7], biomacromolecules [10,17], shoes and gloves. In the mechanical context, chirality leads to the coupling between rotation and bulk deformation, which has inspired many artificial structures with mechanical properties that do not naturally exist, for example, chiral honeycombs with negative Poisson's ratio [11,12,14], chiral acoustic metamaterials [1,4,15,20] and chiral nanoparticle superlattices [18].

A well-known example of chirality is the double-helical structure of DNA molecule [17]. Two antiparallel helical strands of polynucleotides have great contribution to the precise encoding and stable transmission of genetic information. Since its first discovery, the mechanical properties of DNA structure have been extensively investigated. Basic mechanical constants such as Young's modulus, Poisson's ratio, flexural and torsional stiffness have been measured with molecular–biological techniques [6,13], paving the way for the application of classical mechanics in establishing mechanical models of DNA structure [2,3,5,9,16].

Although a large quantity of research has been focused on modeling the mechanical behaviors of the molecular structure of DNA, few engineering structures have been designed following the principle of DNA structure. In this paper, we propose a DNA-inspired helical structure with chirality and study its mechanical behaviors through experimental characterization, theoretical analysis and numerical simulation. Resembling hydrogen bonds between purines and pyrimidines due to complementary base pairing, connections are added between two helices to constrain their relative movement, which are decisive to the chiral deformation mode. Both chiral and non-chiral behaviors of the proposed structures can be quantitively captured by our theoretical and numerical models. The influences of various geometric parameters on the stiffness and deformation mode are discussed. Finally, we present two types of superposed structures that behave differently, showing a high designability of the DNA-inspired structures.

* Corresponding author at: Vehicle Energy & Safety Laboratory (VESL), Beihang University, Beijing, 100191, China.
E-mail address: junxu@buaa.edu.cn (J. Xu).

https://doi.org/10.1016/j.ijmecsci.2019.105025
Received 13 May 2019; Received in revised form 10 July 2019; Accepted 15 July 2019
Available online 15 July 2019

Nomenclature

H	height of DNA-inspired helical structure
N	number of connections
D	diameter of a helix
D_0	original diameter of a helix
R	radius of a helix
R_0	original radius of a helix
d_c	diameter of a connection
d_h	diameter of a helical rod
D_P	diameter of a cylindrical plate
t_P	thickness of a cylindrical plate
A_c	cross-sectional area of a connection
A_h	cross-sectional area of a helical rod
L	length of a helix
L_0	original length of a helix
$I_{p,h}$	polar moment of inertia of cross section of a helical rod
I_h	moment of inertia of cross section of a helical rod
H_n	height of samples for material testing
D_n	diameter of samples for material testing
x, y, z	space coordinates
$\mathbf{r}$	Space vector
ϕ	angular coordinate
φ^h	rotational angle per length of the cross section of the helix rod
φh 0	original rotational angle per length of the cross section of the helix rod
κ	curvature of the helix
κ_0	initial curvature of the helix
Φ^c	angle between the tangent line of the helix and z-x plane
Φc 0	original angle between the tangent line of the helix and z-x plane
σ_{eng}	engineering stress
ϵ_{eng}	engineering strain
E	Young's modulus
G	shear modulus
ν	Poisson's ratio
ϵ_h	strain of helix
F	force
M	moment
δ	displacement
δ_r	relative displacement
θ	rotation
US h	tensile energy of a single helix
UT h	torsional energy of a single helix
UB h	bending energy of a single helix
U_h	total strain energy of a single helix
US c	tensile energy of a single connection
UT c	torsional energy of a single connection
UB c	bending energy of a single connection
U_c	total strain energy of a single connection
U	total strain energy of DNA-inspired helical structure
D_E	average element size
$\bar{I}_1$	the first strain invariant
$\bar{I}_2$	the second strain invariant
U_s	strain energy per unit of reference volume
C_{ij}, D_i	temperature-dependent material parameters
J_{el}	elastic volume strain
$[-]_0$	quantity of benchmark structure
β	height-to-diameter ratio of the structure
β_r	relative height-to-diameter ratio of the structure
α	relative diameter of a connection
AS	axial stiffness of the structure
RS	rotational stiffness of the structure
AS_r	relative axial stiffness of the structure
RS_r	relative rotational stiffness of the structure
λ	spatial periodicity

2. Experimental studies

The geometry of DNA-inspired helical structures and information of samples for experimental studies are provided as below. The schematics of DNA-inspired helical structure is shown in Fig. 1(a). The structure is composed of two intertwined helices with a rotation of 2π, two cylindrical thin plates at the boundaries, and 7 evenly-spaced connections between two helices, resembling hydrogen bonds between purines and pyrimidines of DNA molecular structures. The center lines of two intertwined helices can be analytically described by the following parametric equations

$$\mathbf{r}_1(\phi) = \left[R\cos\phi \quad R\sin\phi \quad \phi H/(2\pi)\right]^{\mathrm{T}} \tag{1a}$$

$$\mathbf{r}_2(\phi) = \left[-R\cos\phi \quad -R\sin\phi \quad \phi H/(2\pi)\right]^{\mathrm{T}} \tag{1b}$$

where $\mathbf{r}_1$ and $\mathbf{r}_2$ represent the space vector of two intertwined helices, respectively.

An important geometrical variation of DNA-inspired helical structure is the number and positions of connections. The angle between neighboring connections is $\pi/4$. The coordinates of connections are denoted as #1–7 and Connection #4 can be regarded as the symmetrical center of all connections. Every two symmetrical connections about Connection #4 are presented in distinguished colors. For convenience, the structure is denoted as N-(…), where N is the number of connections and digits in the parenthesis represent the positions of connections. For example, the structure shown in Fig. 1(a) is denoted as 7-(1,2,3,4,5,6,7). Geometrical dimensions of DNA-inspired helical structure are summarized in Table 1. Samples are additively fabricated with nylon PA2200 using 3D printing device EOS P396 (see Fig. 1(b)), which has a precision of 0.1 mm. Because one end of the structure needs to be fixed to the testing machine in experiments, a protruding is added to the printed samples for the clamping, as is shown in Fig. 1(c).

Material tests are performed using testing machine INSTRON 8801 (see Fig. 2(a)). The height and diameter of samples for material testing are D_n = 12.7 mm and H_n = 25.4 mm respectively, illustrated in Fig. 2(b). To check whether printing direction has an effect on the mechanical properties of 3D-printed constituent material, material tests of samples with different printing directions are conducted. The loading speed is 5 mm/min. The results of material testing are presented in Fig. 2(c–e). Fig. 2(c) and (d) are the results of mechanical properties along (sample #1–4) and perpendicular to (sample #5–8) the printing direction respectively and Fig. 2(e) is a direct comparison between the two. Results in Fig. 2(c) and (d) shows that material testing has good repeatability, and it can be concluded in Fig. 2(e) that mechanical properties of nylon PA2200 are independent of printing direction and thus can be regarded as isotropic. Only Young's modulus and Poisson's ratio are obtained as E = 1200 MPa and ν = 0.35 based on material tests for further theoretical and numerical investigations, due to that the material strain of DNA-inspired helical structure compressed by 30% is very small and the stress–strain curve is still linear as shown in Fig. S1.

Table 1
Geometrical dimensions of DNA-inspired helical structure (unit: mm).

H	D	d_c	d_h	D_P	t_P
100	48	5.6	5.6	60	10

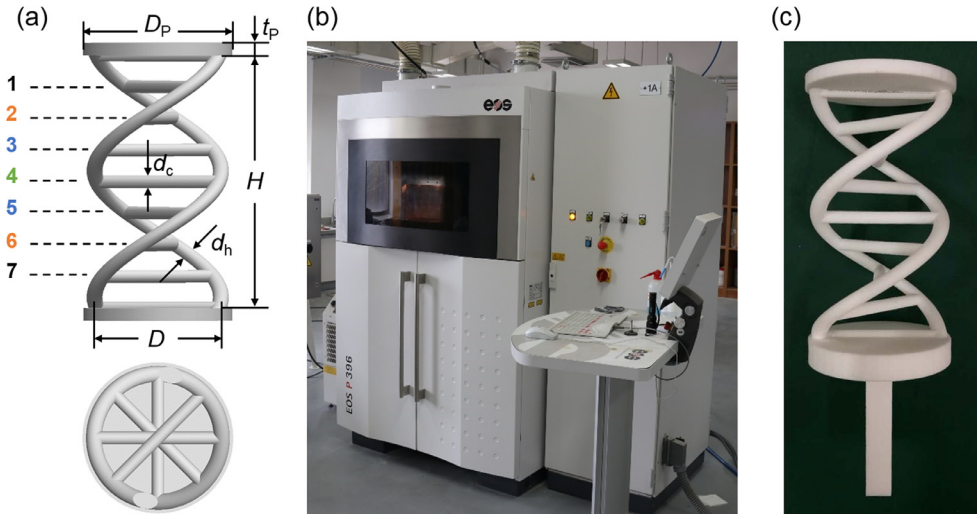

Fig. 1. Schematics and fabrication of DNA-inspired helical structure. (a) Schematics of DNA-inspired helical structure. (b) 3D printing device EOS P396. (c) A 3D-printed sample of DNA-inspired helical structure.

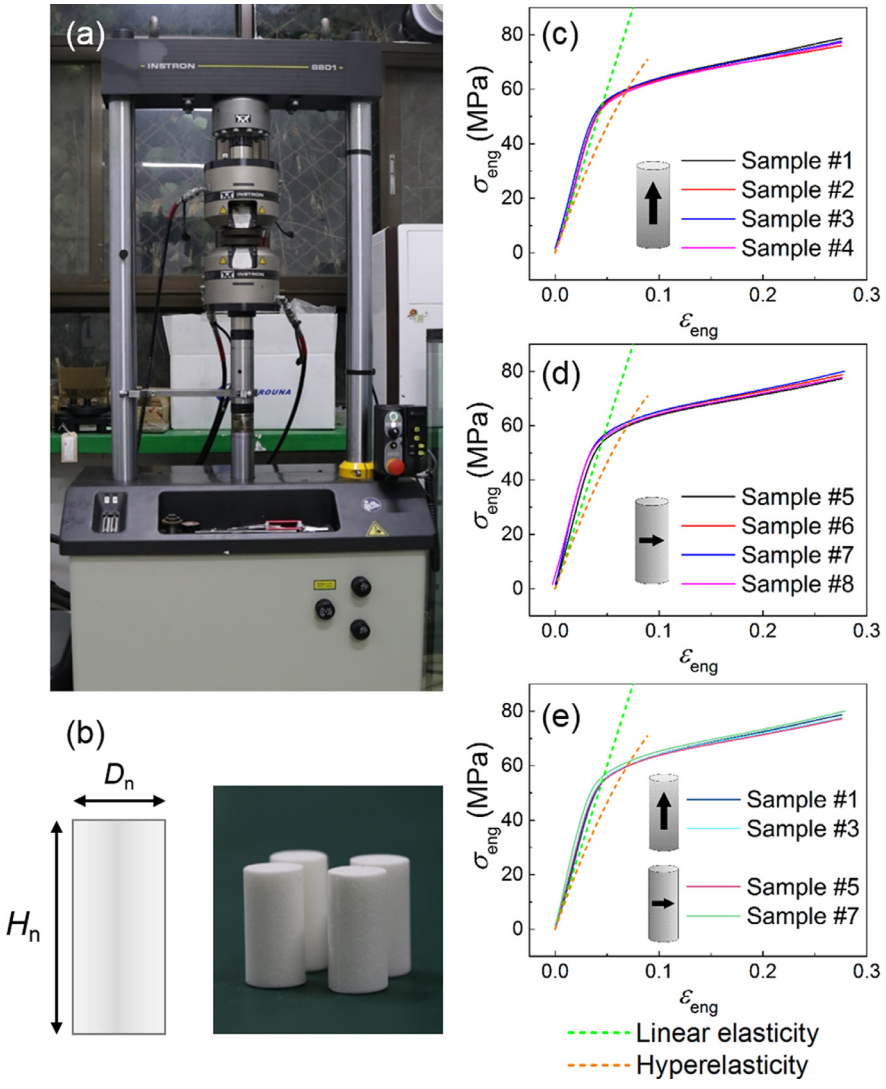

Fig. 2. Material testing of nylon PA2200. (a) Material testing device INSTRON 8801. (b) Samples for material testing. (c–e) Material testing results of samples with different printing directions. Stress–strain curves predicted by constitutive relations based on linear elasticity and hyperelasticity are also provided.

Compression tests of DNA-inspired helical structures are performed using testing machine INSTRON 2345 (see Fig. 3(a)). To investigate the chiral behavior of the structure, the degree of freedom for rotation cannot be eliminated. To this end, one end of sample is fixed to the testing machine by clamping, while the other end is loaded with a flat compressor. To minimize the influence of friction between compressor and upper plate on the mechanical response, lubricating grease is applied at this interface to make sure the free rotation. A small camera is placed on the upper face of the lower plate of the sample to record the rotational movement of the structure. The mechanical behaviors of three

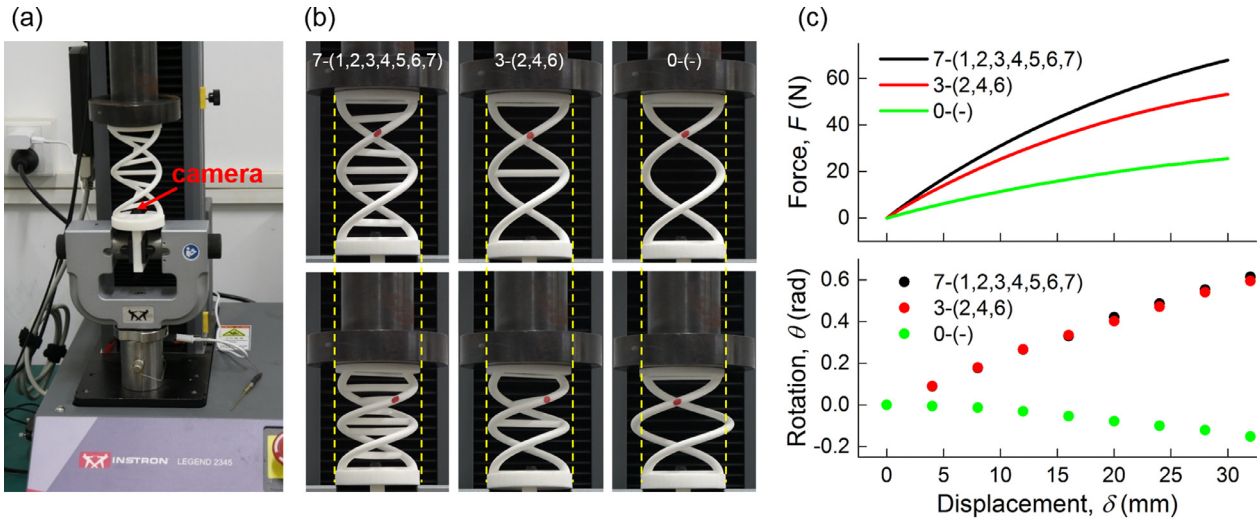

Fig. 3. Compression tests of DNA-inspired helical structures. (a) Experimental setup of compression tests. (b) Deformations of different DNA-inspired helical structures during compression tests. (c) Force–displacement and rotation–displacement relations of different DNA-inspired helical structures.

types of structure are experimentally studied, namely, 7-(1,2,3,4,5,6,7), 3-(2,4,6) and 0-(–). The loading speed is 2 mm/min, regarded as quasi-static loading.

Snapshots of compression tests of these structures are presented in Fig. 3(b). As is shown, upon compressive loading, 7-(1,2,3,4,5,6,7) and 3-(2,4,6) exhibit no lateral dilation, and from the red marker on the helical rod we can clearly see that the two structures rotate over approximately a same angle of the same direction, corresponding to chiral deformation. However, 0-(–) rotates over a relatively small angle of the opposite direction and dilates laterally. Therefore, connections are decisive to the deformation mode. Downward and counterclockwise looking down from the compressor are taken as positive directions of displacement and rotation. The experimental results of force–displacement and rotation–displacement relations of the three types of the structure are presented in Fig. 3(c). Structural stiffness increases with the number of connections. Rotation–displacement relations of 7-(1,2,3,4,5,6,7) and 3-(2,4,6) are almost identical, suggesting that these two types in fact have the same chiral deformation mode.

3. Theoretical and numerical models

3.1. Theoretical modeling

The principle of minimum potential energy was employed to theoretically study the mechanical behaviors of DNA-inspired structure. When the structure is subjected to axial and torsional loading, total potential energy of the system is expressed as

$$\Pi = U - F\delta - M\theta \tag{2}$$

whereas U represents the strain energy of the structure, which is composed of tensile, torsional and bending energy of two helices and N connections. To simplify the following theoretical analysis, the total rotational angle of one helix after deformation is represented as $\gamma = \theta + 2\pi$. Then, the configurations of the DNA-inspired structure can be described by R, γ, δ, as well as the initial geometry parameters, and the principle of minimum potential energy gives

$$d\Pi = \frac{\partial U}{\partial R} dR + \left(\frac{\partial U}{\partial \delta} - F\right) d\delta + \left(\frac{\partial U}{\partial \gamma} - M\right) d\gamma = 0 \tag{3}$$

thus, the governing equations are

$$\frac{\partial U}{\partial R} = 0 \tag{4}$$

$$\frac{\partial U}{\partial \delta} - F = 0 \tag{5}$$

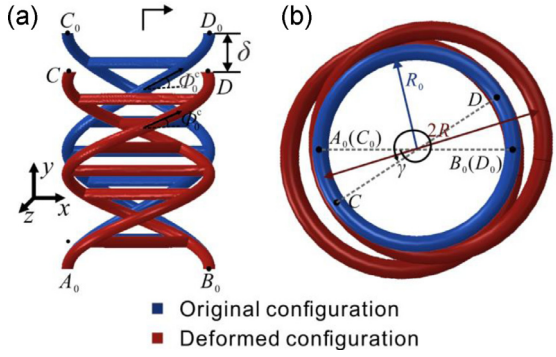

Fig. 4. Schematic plot of the deformation of the DNA-inspired structure for on period. (a) Front view of the DNA-inspired structure before and after deformation. (b) Top view of the helix.

$$\frac{\partial U}{\partial \gamma} - M = 0 \tag{6}$$

The mechanical behaviors of the DNA-inspired structure could be determined by Eqs. (4)–(6).

Schematic plot of the deformation of the DNA-inspired structure is given in Fig. 4. According to Fig. 4, strain energy of one period of the DNA-inspired helical structure can be expressed as

$$U = 2U_{\mathrm{h}} + NU_{\mathrm{c}} \tag{7}$$

in which U_{h} and U_{c} represent the strain energy of a single helix and a single connection, respectively. U_{h} and U_{c} can then be further expressed as

$$U_{\mathrm{h}} = U_{\mathrm{h}}^{\mathrm{S}} + U_{\mathrm{h}}^{\mathrm{T}} + U_{\mathrm{h}}^{\mathrm{B}} \tag{8}$$

$$U_{\mathrm{c}} = U_{\mathrm{c}}^{\mathrm{S}} + U_{\mathrm{c}}^{\mathrm{B}} + U_{\mathrm{c}}^{\mathrm{T}} \tag{9}$$

where $U_{\mathrm{h}}{}^{\mathrm{S}}$, $U_{\mathrm{h}}{}^{\mathrm{T}}$ and $U_{\mathrm{h}}{}^{\mathrm{B}}$ represent the tensile, twisting and bending energy of a single helix, respectively, while $U_{\mathrm{c}}{}^{\mathrm{S}}$, $U_{\mathrm{c}}{}^{\mathrm{T}}$ and $U_{\mathrm{c}}{}^{\mathrm{B}}$ represent the above forms of energy of a connection, respectively. Based on the hypothesis of linear elasticity, the aforementioned forms of energy can be analytically expressed as

$$U_{\mathrm{h}}^{\mathrm{S}} = \frac{1}{2} E\varepsilon_{\mathrm{h}}^2 L_0 A_{\mathrm{h}} = \frac{EA_{\mathrm{h}}}{2L_0}\left(L - L_0\right)^2 \tag{10}$$

$$U_{\mathrm{h}}^{\mathrm{T}} = \frac{1}{2} GI_{\mathrm{p,h}}\left(\varphi^{\mathrm{h}} - \varphi_0^{\mathrm{h}}\right)^2 L_0 \tag{11}$$

$$U_{\mathrm{h}}^{\mathrm{B}} = \frac{1}{2} E I_{\mathrm{h}} (\kappa - \kappa_0)^2 L_0 \tag{12}$$

$$U_{\mathrm{c}}^{\mathrm{S}} = \frac{1}{2} E \varepsilon_{\mathrm{c}}^2 (2R_0) A_{\mathrm{c}} = \frac{E A_{\mathrm{c}}}{R_0} (R - R_0)^2 \tag{13}$$

$$U_{\mathrm{c}}^{\mathrm{T}} = \frac{1}{2} G I_{\mathrm{p,c}} \left(\frac{\Phi^{\mathrm{c}} - \Phi_0^{\mathrm{c}}}{R} \right)^2 (2R_0) \tag{14}$$

$$U_{\mathrm{c}}^{\mathrm{B}} = 0 \tag{15}$$

where $I_{\mathrm{p,h}} = A_{\mathrm{h}}^2/(2\pi)$, $I_{\mathrm{h}} = A_{\mathrm{h}}^2/(4\pi)$ and $I_{\mathrm{p,c}} = A_{\mathrm{c}}^2/(2\pi)$ are the polar moment, moment of inertia of cross section of the helical rod and polar moment of inertia of cross section of the connection, respectively. Here, the lengths of the helix before and after deformation are

$$L_0^2 = (2\pi R_0)^2 + H^2 \tag{16a}$$

$$L^2 = (\gamma R)^2 + (H - \delta)^2. \tag{16b}$$

According to the previous literatures, the rotational angle per length of the cross section of the helix rod before and after deformation are

$$\varphi_0^{\mathrm{h}} = 2\pi H / L_0^2 \tag{17a}$$

$$\varphi^{\mathrm{h}} = \gamma (H - \delta) / L^2 \tag{17b}$$

And the curvatures of the helix before and after deformation are

$$\kappa_0 = 4\pi^2 R_0 / L_0^2 \tag{18a}$$

$$\kappa = \gamma^2 R / L^2. \tag{18b}$$

Φ_0^{c} and Φ^{c} are the angles between the tangent line of the helix and z–x plane before and after deformation which determine the torsion of the connections,

$$\sin\left(\Phi_0^{\mathrm{c}}\right) = \frac{H}{L_0} \tag{19a}$$

$$\sin\left(\Phi^{\mathrm{c}}\right) = \frac{H - \delta}{L}. \tag{19b}$$

Combining Eqs. (7)–19a) and (19b), the partial derivatives in Eqs. (3)–((6) can be further expressed as

$$\begin{aligned}\frac{\partial U}{\partial R} &= 2EA_{\mathrm{h}}\gamma^2 R\left(\frac{1}{L_0} - \frac{1}{L}\right) + \frac{2NEA_{\mathrm{c}}}{R_0}(R - R_0) \\ &\quad - \frac{2GA_{\mathrm{h}}^2 L_0 (H - \delta)\gamma^3 R}{\pi L^4}\left[\frac{\gamma(H - \delta)}{L^2} - \frac{2\pi H}{L_0^2}\right] \\ &\quad - \frac{NGA_{\mathrm{c}}^2 R_0}{\pi R^3}\left\{\frac{R\gamma(H - \delta)}{L^2} + \arcsin\left(\frac{H - \delta}{L}\right) - \arcsin\left(\frac{H}{L_0}\right)\right\} \\ &\quad \times \left[\arcsin\left(\frac{H - \delta}{L}\right) - \arcsin\left(\frac{H}{L_0}\right)\right] \\ &\quad + \frac{EA_{\mathrm{h}}^2 L_0 \gamma^2 (L^2 - 2R^2\gamma^2)}{2\pi L^4}\left(\frac{R\gamma^2}{L^2} - \frac{4\pi^2 R_0}{L_0^2}\right)\end{aligned} \tag{20}$$

$$\begin{aligned}\frac{\partial U}{\partial \delta} &= -2EA_{\mathrm{h}}(H - \delta)\left(\frac{1}{L_0} - \frac{1}{L}\right) \\ &\quad - \frac{GA_{\mathrm{h}}^2 L_0 \gamma \left[2(H - \delta)^2 - L^2\right]}{\pi L^4}\left[\frac{\gamma(H - \delta)}{L^2} - \frac{2\pi H}{L_0^2}\right] \\ &\quad - \frac{NGA_{\mathrm{c}}^2 R_0 \theta}{\pi R L^2}\left[\arcsin\left(\frac{H - \delta}{L}\right) - \arcsin\left(\frac{H}{L_0}\right)\right] \\ &\quad + \frac{EA_{\mathrm{h}}^2 L_0 R\gamma^2 (H - \delta)}{\pi L^4}\left(\frac{R\gamma^2}{L^2} - \frac{4\pi^2 R_0}{L_0^2}\right)\end{aligned} \tag{21}$$

$$\begin{aligned}\frac{\partial U}{\partial \gamma} &= 2EA_{\mathrm{h}}\gamma^2 R\left(\frac{1}{L_0} - \frac{1}{L}\right) \\ &\quad - \frac{GA_{\mathrm{h}}^2 L_0 (H - \delta)\left(2\gamma^2 R^2 - L^2\right)}{\pi L^4}\left[\frac{\gamma(H - \delta)}{L^2} - \frac{2\pi H}{L_0^2}\right] \\ &\quad - \frac{NGA_{\mathrm{c}}^2 R_0 (H - \delta)}{\pi R L^2} \times \left[\arcsin\left(\frac{H - \delta}{L}\right) - \arcsin\left(\frac{H}{L_0}\right)\right] \\ &\quad + \frac{EA_{\mathrm{h}}^2 L_0 R\gamma \left(L^2 - 2R^2\gamma^2\right)}{\pi L^4}\left(\frac{R\gamma^2}{L^2} - \frac{4\pi^2 R_0}{L_0^2}\right)\end{aligned} \tag{22}$$

In the experiment, axial loading is applied and the DNA-inspired structure is free of rotation which gives $M = 0$. Substituting $\partial U/\partial\gamma = 0$ into Eq. (22), the relations of F, R, θ to the axial compression displacement δ are obtained by numerical solving Eqs. (20)–(22). Besides, the torsional loading is also applied to the DNA-inspired structure in our finite element (FE) simulations and the DNA-inspired structure is free of deformation in the axial direction. Substituting $\partial U/\partial\delta = 0$ into Eq. (21), the relations of M, R, δ to the rotational angle θ are obtained by numerical solving Eqs. (20)–(22). The comparisons of theoretical predictions to that of the experimental results and FE simulation results are given in the following sections which show very good agreements.

According to experimental results, connections between two intertwined helices are decisive to the chiral deformation mode of the structure. Namely, neglecting the elongation or contraction of connections due to elastic deformation, connections serve as a constraint that keeps the relatively spacing of two helices constant. Therefore, the deformation pattern of the structure becomes helical movement and thus the axial and rotational deformation of the structure are dependent, suggesting a one-degree-of-freedom system. Neglecting the elongation or contraction of helical rods due to elastic deformation, the geometric relation of helical movement corresponding to chirality can be given as

$$(2\pi R_0)^2 + H^2 = \left[(2\pi + \theta)R_0\right]^2 + (H - \delta)^2 \tag{23}$$

3.2. Numerical modeling

Numerical calculations are performed based on finite element (FE) methods using commercial software ABAQUS. DNA-inspired helical structure is meshed with 10-node quadratic tetrahedron elements (element type in ABAQUS: C3D10 (ABAQUS 6.14 Documentation)). Two types of constitutive relation are used in the numerical model, namely, linear elasticity and hyperelasticity. For linear elastic constitutive relation, material parameters are set as $E = 1200$ MPa and $\nu = 0.35$, consistent with material testing results. For hyperelastic constitutive relation, polynomial form of the strain energy is applied, expressed as

$$\begin{aligned}U_{\mathrm{s}} &= C_{10}(\bar{I}_1 - 3) + C_{01}(\bar{I}_2 - 3) + C_{20}(\bar{I}_1 - 3)^2 + C_{11}(\bar{I}_1 - 3)(\bar{I}_2 - 3) \\ &\quad + C_{02}(\bar{I}_2 - 3)^2 + \sum_{i=1}^{2} \frac{1}{D_i}(J_{\mathrm{el}} - 1)^{2i}\end{aligned} \tag{24}$$

Material constants are computed based on material testing data. Stress–strain curves predicted based on these two constitutive relations are provided in Fig. 2(c–e). The boundary conditions of the FE model are illustrated in Fig. 4(a). The lower plate of the structure is fixed, while the upper plate is free to translate along and rotate about Y axis and Y displacement of the upper plate is set as 30 mm to achieve loading (Fig. 5).

Firstly, compression tests are performed numerically based on average element sizes of ~2.3 mm, ~1.3 mm and ~1.0 mm. It is shown that when the element size downsizes from ~1.3 mm to ~1.0 mm, the deviation of numerical results is negligibly small, thus validating the convergence of the FE model. For the efficiency of numerical calculation, structures are meshed with elements with an average size of ~1.3 mm in further FE simulations.

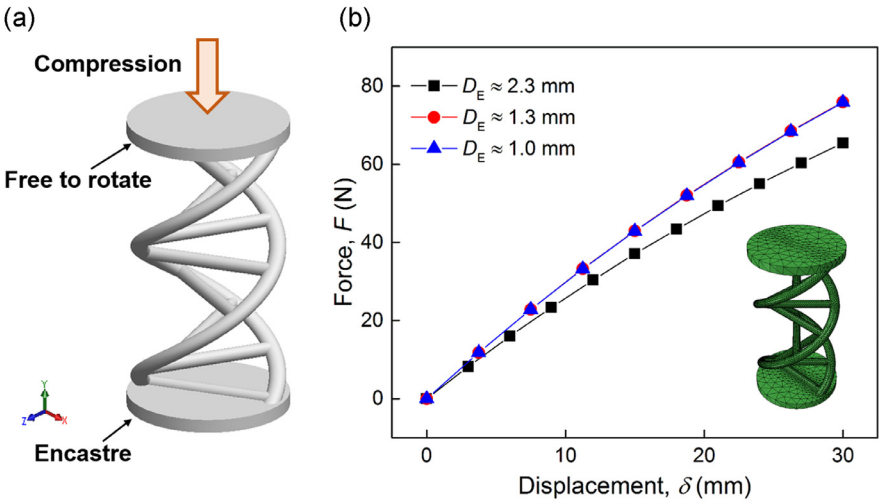

Fig. 5. Descriptions of FE model. (a) Illustration of boundary conditions. (b) Numerical compression tests based on different average element sizes as the convergence validation of FE model.

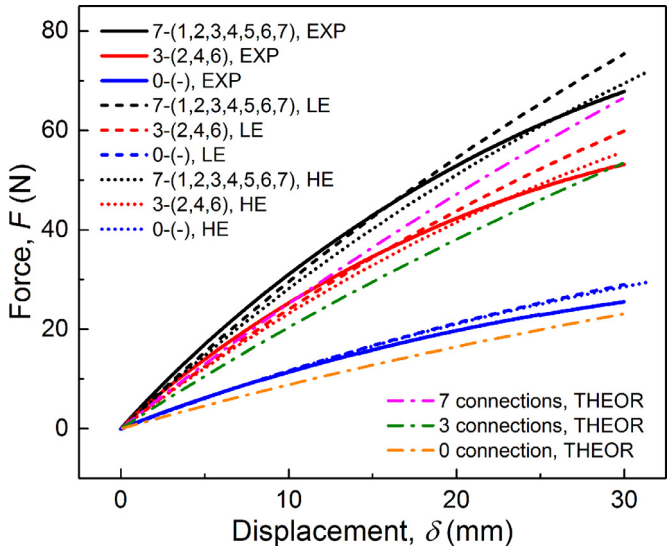

Fig. 6. Experimental results (EXP), numerical results of FE calculations based on linear elasticity (LE) and hyperelasticity (HE), and theoretical predictions (THEOR) of three types of DNA-inspired helical structures subject to compressive loading.

4. Results

Experimental and numerical results of force-displacement relations of DNA-inspired helical structures subject to compressive loading, as well as theoretical predictions, are presented in Fig. 6. It is shown that these results generally yield good agreement. Because there exhibits no large deviation between the numerical results based on linear elasticity and hyperelasticity, for the convenience of further analysis and discussion, linear elastic constitutive relation is used in the numerical studies afterwards. Note that theoretical predictions are slightly lower than other results. This could be explained by the fact that the boundary plates can have an effect on the increase of overall stiffness of the structure, which is not taken into account in the theoretical model. We will later show that when the structure becomes longer where the boundary effect becomes less significant, the force-displacement results converge to the theoretical predictions.

Because the chiral deformation of DNA-inspired helical structure is a one-degree-of-freedom problem, for an axial loading over some displacement, same structural deformation could be realized when the structure is subject to torsional loading over a certain rotation. Suppose this displacement is 30 mm downward, comparison of FE-calculated morphologies of DNA-inspired helical structure subject to axial loading, torsional loading and the prediction of geometric relation is shown in Fig. 7(a), where space coordinates of nodes of FE model after deformation are extracted to reconstruct the deformed shapes. It is shown that FE-calculated morphologies are in good accordance with the prediction

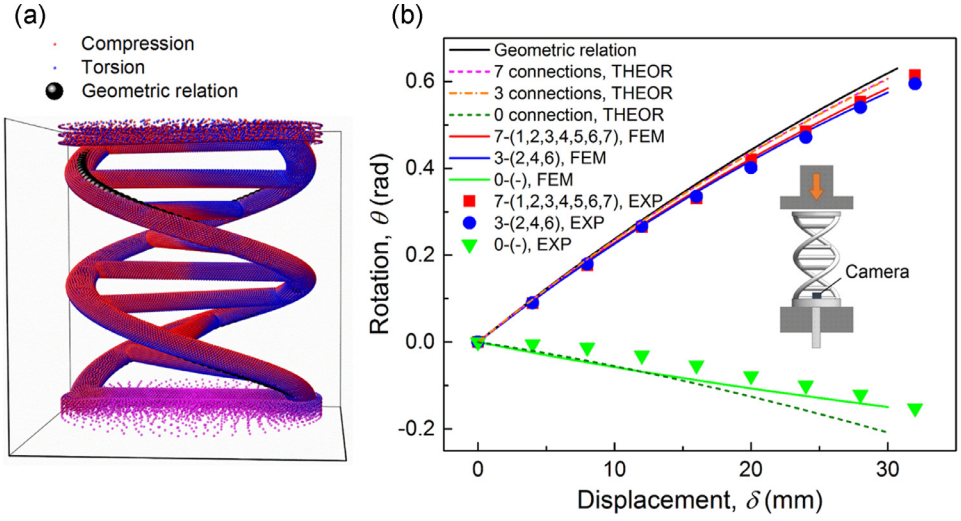

Fig. 7. Deformation predictions based on FE calculations, geometric relation, and theoretical model. (a) Comparison of FE-calculated morphologies of DNA-inspired helical structure subject to compression and torsion and geometric relation. (b) Rotation–displacement relation based on the predictions of geometric relation and theoretical model and numerical and experimental results.

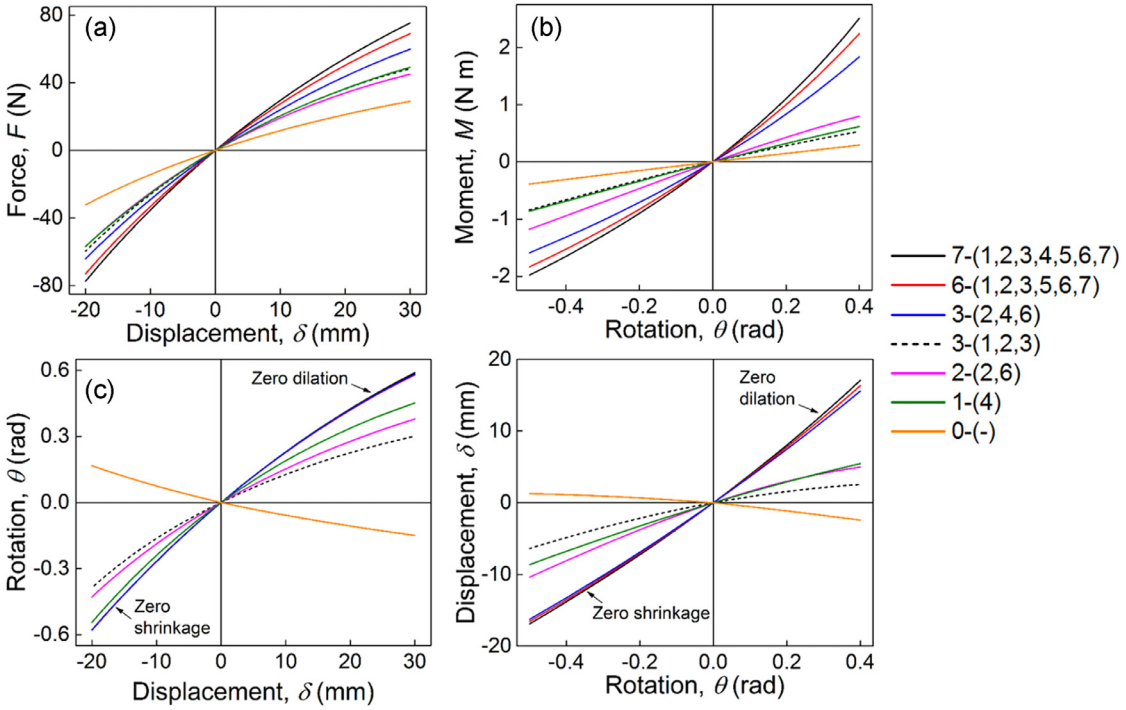

Fig. 8. FE results of various structures under different loading conditions. (a) Force-displacement relations subject to axial loading. (b) Moment–rotation relations subject to torsional loading. (c) Rotation–displacement relations subject to axial loading. (d) Displacement–rotation relations subject to torsional loading.

of geometric relation. Note that there is a small noncoincidence between the deformed shapes caused by compressive and torsional loadings. This could be accounted for by the difference of strain fields due to different loading conditions. Deformation based on FE calculation is nonuniform because the structure is stiffer near the boundary plates, while the prediction of geometric relation yields uniform deformation. This results in a minor deviation between the FE-calculated and geometrically predicted deformed shapes near the boundary. Experimental and numerical results of rotation–displacement relation, as well as the predictions based on geometric relation and theoretical model, are presented in Fig. 7(b), generally showing a good consistency. Upon relatively large displacement ($\delta > 20$ mm), theoretical prediction of structure with no connection begins to deviate from numerical and experimental results. This is because for this type of structure, large deflection of helical rods may occur, dissatisfying the hypothesis of small deformation of the theoretical model.

Next, numerical calculations are performed based on this model to investigate the mechanical responses of more types of structures under various loading conditions. Force-displacement relations and moment–rotation relations of various structures are presented in Fig. 8(a) and (b). Results show that both axial and rotational stiffness increase with the number of connections. For structures with unsymmetrically-arranged connections, for example, 3-(1,2,3), its axial and rotational stiffness are significantly inferior to its symmetrical counterpart, i.e. 3-(2,4,6). Rotation–displacement relations under axial and torsional loading are presented in Fig. 8(c) and (d). Results show that as the number of connections increases, deformation modes tend to converge, corresponding to chiral deformation. In this case, the structures exhibit zero lateral dilation subject to compression and counterclockwise torsion, and exhibit zero lateral shrinkage subject to tension and clockwise torsion, which can be called stable deformation modes. For structure with unsymmetrically-arranged connections 3-(1,2,3), unlike its symmetrical counterpart 3-(2,4,6), its rotation–displacement relation does not reach the stable deformation modes.

For stable deformation modes with chirality, different loading conditions can result in the same deformed shape. Taking 7-(1,2,3,4,5,6,7) as an example, predictions based on geometric relation and theoretical model and numerical results of rotation–displacement relation of under compression, tension and counterclockwise/clockwise torsion are presented in Fig. 9, showing a good consistency.

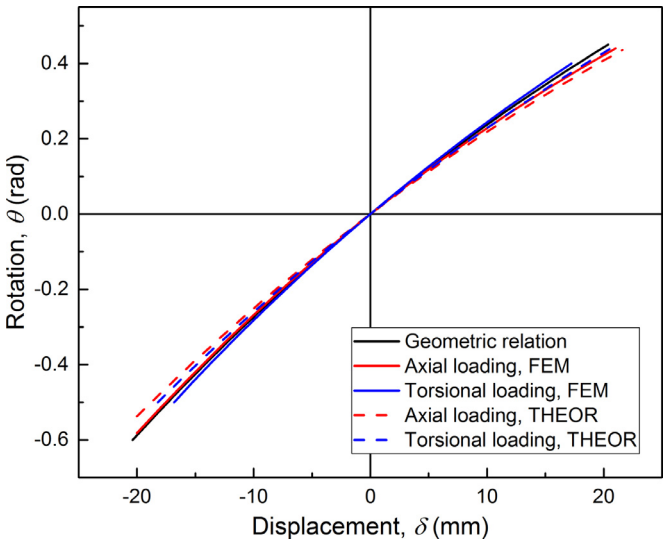

Fig. 9. Rotation–displacement relations of 7-(1,2,3,4,5,6,7) under different loading conditions based on geometric relation, FE calculation and theoretical model.

5. Discussion

5.1. Governing factors on structural stiffness

The structural stiffness of DNA-inspired helical structure can be tuned by geometrical variation. It has been shown that the structure

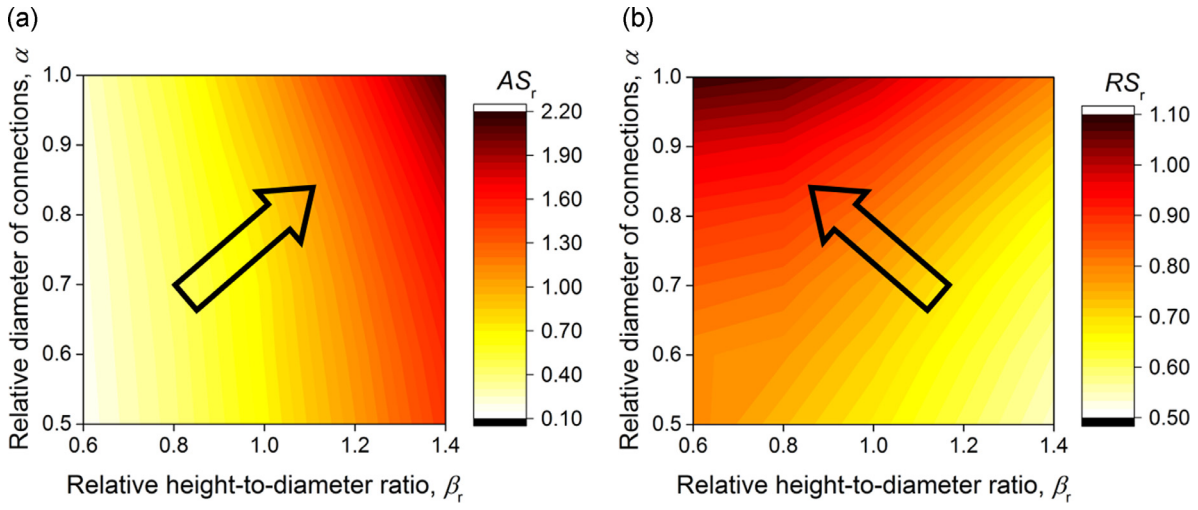

Fig. 10. Effect of height-to-diameter ratio and relative diameter of connections on (a) axial and (b) rotational stiffness.

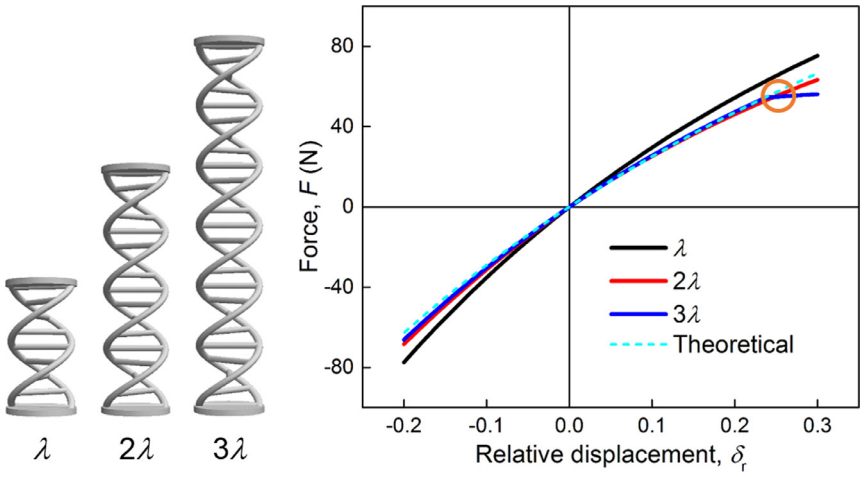

Fig. 11. The influence of spatial periodicity on force–displacement relation. The occurrence of buckling behavior is circled.

becomes stiffer as the number of connections increase and that unsymmetrical arrangement of connections deteriorates both axial and rotational stiffness. The influences of height-to-diameter ratio and diameter of connections on structural stiffness are quantitatively discussed based on 7-(1,2,3,4,5,6,7) with a stable chirality deformation mode as follows. Nondimensionalized quantities relative height-to-diameter ratio β_r and relative diameter of connections α are introduced, defined as

$$\beta_r = \beta/[\beta]_0 = \frac{H/D_0}{[H/D_0]_0} \tag{25}$$

$$\alpha = d_c/[d_c]_0 \tag{26}$$

Because the diameter of connections cannot exceed the diameter of helical rods, we have $\alpha \in (0, 1]$. Structural stiffness is quantified by axial and rotational stiffness at $\delta = 0$ and $\theta = 0$ as

$$AS = \left.\frac{dF}{d\delta_r}\right|_{\delta_r=0} \tag{27}$$

$$RS = \left.\frac{dM}{d\theta}\right|_{\theta=0} \tag{28}$$

Relative axial and rotational stiffness are defined as $AS_r = AS/[AS]_0$ and $RS_r = RS/[RS]_0$ respectively. Results are presented in the form of α–β_r maps in Fig. 10. It can be observed that both axial and rotational stiffness are in proportion to the diameter of connections. This conclusion is comprehensible because the increase of diameter of connections results in larger axial and rotational stiffness of connections, adding to the total strain energy of the structure upon a certain structural deformation. However, as height-to-diameter ratio increases, axial stiffness becomes higher while rotational stiffness becomes lower. To understand this graphically, "thinner" structures are more resistant to axial loading but more vulnerable to rotational loading, and vice versa. This suggests that balancing axial and rotational stiffness can be possibly achieved by tuning height-to-diameter ratio.

The influence of spatial periodicity on force-displacement relation is studied as below. Relative displacement is defined as $\delta_r = \delta/H$. Compression and tension tests are performed numerically with structures of λ, 2λ and 3λ, and are compared with theoretical predictions. Results in Fig. 10 show that shorter structure has higher stiffness due to the strengthening of boundary plates, and that when the structure becomes longer, force-displacement relation converges to the prediction of theoretical model, in which case the boundary effect becomes less significant. Note that for the structure of 3λ, Euler buckling behavior can occur, as is circled in Fig. 11. The buckling analysis of DNA-inspired helical structures will be covered in our future work.

5.2. Governing factors on deformation mode

Deformation mode dominates the mechanical behavior such that influences of height-to-diameter ratio, diameter of connections, spatial

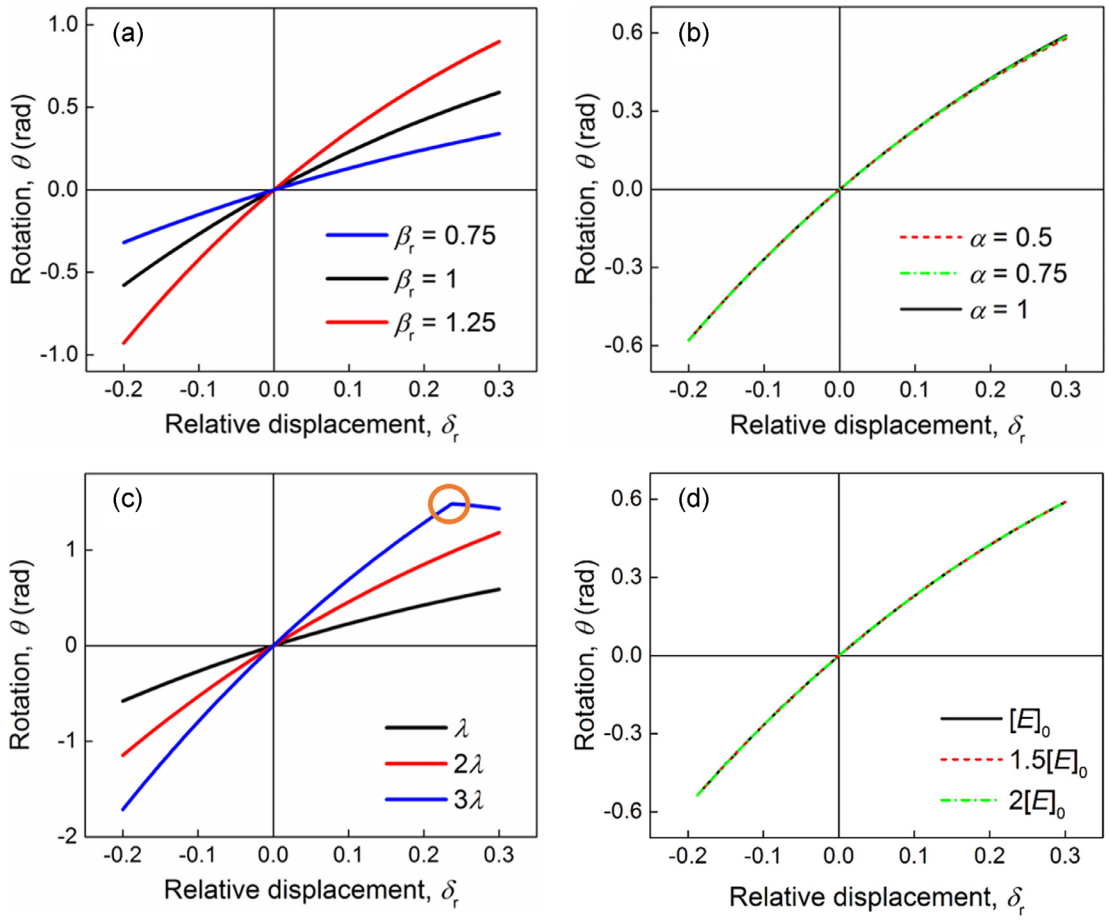

Fig. 12. Influences of (a) height-to-diameter ratio, (b) diameter of connections, (c) spatial periodicity, and (d) Young's modulus of the constituent material on rotation–displacement relation. The occurrence of buckling behavior is circled.

periodicity, as well as Young's modulus of the constituent material on the chiral deformation mode of DNA-inspired helical structure are discussed as follows. Numerical calculations are still based on 7-(1,2,3,4,5,6,7) and chiral deformations are induced by axial loading. Fig. 11(a) presents the rotation–displacement relations of $\beta_r = 0.75$, 1 and 1.25, showing that for higher height-to-diameter ratio, upon axial loading to a certain relative displacement, the structure rotates over a larger angle. This suggests that chirality becomes stronger as the structure becomes "thinner". Fig. 11(b) presented the results of $\alpha = 0.5$, 0.75 and 1, indicating that diameter of connections in fact has little effect on the rotation–displacement relation. Although the decrease of diameter of connections can lower the overall structural stiffness, the constraining function of connections still exists. Fig. 11(c) gives the rotation–displacement of different spatial periodicity λ, 2λ and 3λ, showing that structure with higher spatial periodicity rotates more upon axial loading to a certain relative displacement, though Euler buckling can happen. Different from the effect of height-to-diameter ratio, this could be explained by the superposition of chirality of spatial periods. Finally, Fig. 11(d) investigates the deformation mode of $[E]_0$, $1.5[E]_0$ and $2[E]_0$, indicating that in the linear elastic FE model, Young's modulus of the constituent material does not affect the chiral deformation mode. Above analysis brings lights on how geometrical/material parameters affect the stable chiral deformation mode of DNA-inspired helical structures.

5.3. Superposed structures

Lastly, the mechanical behaviors of DNA-inspired helical superposed structures with translational and central symmetry (denoted as TS and CS respectively) are investigated, of which the bandgap properties are discussed in Ref. [19]. The superposed structures are composed of a top plate, a middle plate, a bottom plate, and two double-helical parts based on 7-(1,2,3,4,5,6,7). The bottom plate is fixed and loads are exerted to the top plate. The only difference lies in the double-helical parts. In the TS superposed structure, two double-helical parts have the same rotational direction, while in the CS superposed structure, they have an opposite rotational direction. The schematics are shown in Fig. 12(a) (Fig. 13).

Axial and torsional loading are applied to the top plates to investigates the mechanical responses of the superposed structures, as are presented in Fig. 12(b–e). Results in Fig. 12(b) and (c) shows that their force-displacement and moment–rotation relations have little difference, indicating that symmetrical property actually has little effect on the overall structural stiffness. On the other hand, it can be observed from Fig. 12(d) and (e) that the deformation modes of two superposed structures are completely different. Upon the same axial loading, the middle plates of TS and CS superposed structures rotate over a same angle. Interestingly, in contrast to TS superposed structure, the top plate of CS superposed structure does not rotate upon axial loading. Upon the same torsional loading, the middle plates of TS and CS superposed structures translate over a same displacement. However, the top plate of CS superposed structure does not translate. This deformation mode can be explained by the cancellation of chirality of two double-helical parts of CS superposed structure due to its symmetrical property. The proposal of superposed structures greatly expands to the designing freedom of DNA-inspired helical structures.

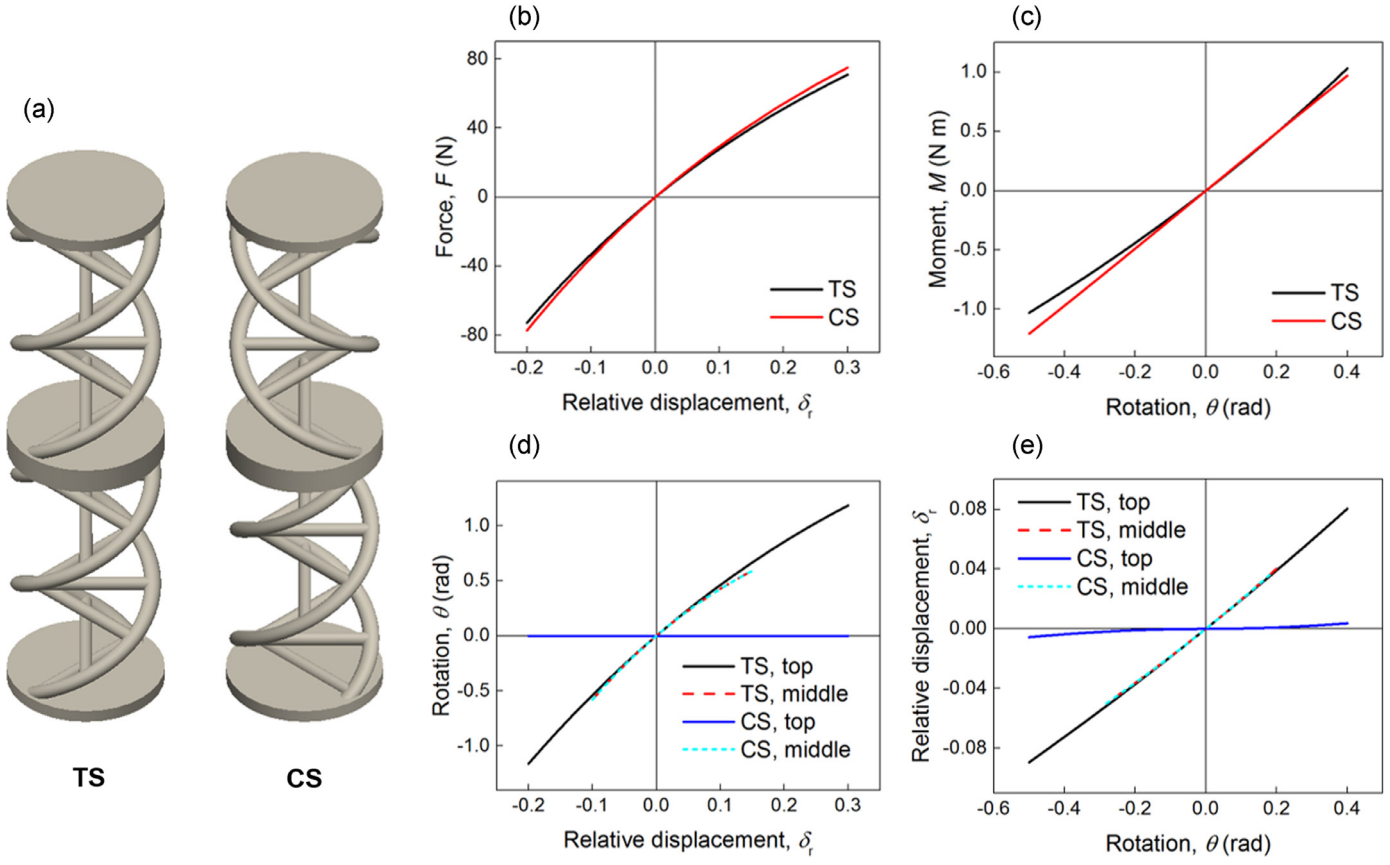

Fig. 13. Mechanical behaviors of DNA-inspired helical superposed structures with translational and central symmetry. (a) Schematics of DNA-inspired helical superposed structures with translational and central symmetry. (b) Force–displacement relations subject to axial loading. (c) Moment-rotation relations subject to torsional loading. (d) Rotation–displacement relations subject to axial loading. (e) Displacement–rotation relations subject to torsional loading.

6. Conclusion

In this work, we present a design of helical structure with chirality and study its mechanical behaviors experimentally, theoretically and numerically. We find that connections between two intertwined helices are decisive to the stable chiral deformation mode and both chiral and non-chiral behaviors of the structures can be quantitively captured by our theoretical and numerical models. The influences of various geometric parameters on the stiffness and deformation mode are discussed. Finally, we present two types of superposed structures that behave differently, showing a high designability of the DNA-inspired structures. This study exploits the chirality of biological structures and uses it in structural design with novel mechanical properties, which may facilitate the development of bio-inspired mechanical metamaterials, impact energy absorbers and multi-functional composite materials.

Acknowledgments

This work is financially supported by Fundamental Research Funds for the Central Universities, Beihang University and start-up funds of "The Recruitment Program of Global Experts" awardee (YWF-17-BJ-Y-28), Beihang University, Beijing Municipal Science & Technology Commission (Grant No. Z161100001416006) and Opening fund of State Key Laboratory for Strength and Vibration of Mechanical Structures, Xi'an Jiaotong University (SV2015-KF-07, SV2016-KF-20).

Supplementary materials

Supplementary material associated with this article can be found, in the online version, at doi:10.1016/j.ijmecsci.2019.105025.

References

[1] Bacigalupo A, Gambarotta L. Simplified modelling of chiral lattice materials with local resonators. Int J Solids Struct 2016;83:126–41.
[2] Benham CJ. Elastic model of supercoiling. Proc Natl Acad Sci USA 1977;74:2397–401.
[3] Bouchiat C, Mézard M. Elasticity model of a supercoiled DNA molecule. Phys Rev Lett 1998;80:1556–9.
[4] Chen H, Fung KH, Ma H, Chan CT. Polarization gaps and negative group velocity in chiral phononic crystals: layer multiple scattering method. Phys Rev B 2008;77:224304.
[5] Coleman BD, Swigon D, Tobias I. Elastic stability of DNA configurations. II. Supercoiled plasmids with self-contact. Phys Rev E 2000;61:759–70.
[6] Hagerman PJ. Flexibility of DNA. Ann Rev Biophys Biophys Chern 1988;17:265–86.
[7] Iijima S. Helical microtubules of graphitic carbon. Nature 1991;354:56–8.
[8] Kelvin WTB. The molecular tactics of a crystal. Clarendon Press; 1894.
[9] Liu Y. Nonlinear mechanics of thin elastic rod: theoretical basis of mechanical model of DNA. Beijing: Tsinghua Press; 2006.
[10] O'Shea EK, Klemm JD, Kim PS, Alber T. X-ray structure of the GCN4 leucine zipper, a two-stranded, parallel coiled coil. Science 1991;254:539–44.
[11] Prall D, Lakes RS. Properties of a chiral honeycomb with a poisson's ratio of — 1. Int J Mech Sci 1997;39:305–14.
[12] Scarpa F, Blain S, Lew T, Perrott D, Ruzzene M, Yates JR. Elastic buckling of hexagonal chiral cell honeycombs. Compos Pt A-Appl Sci Manuf 2007;38:280–9.
[13] Smith SB, Finzi L, Bustamante C. Direct mechanical measurements of the elasticity of single DNA molecules by using magnetic beads. Science 1992;258:1122–6.
[14] Spadoni A, Ruzzene M. Elasto-static micropolar behavior of a chiral auxetic lattice. J Mech Phys Solids 2012;60:156–71.
[15] Spadoni A, Ruzzene M, Gonella S, Scarpa F. Phononic properties of hexagonal chiral lattices. Wave Motion 2009;46:435–50.
[16] Tobias I, Swigon D, Coleman BD. Elastic stability of DNA configurations. I. General theory. Phys Rev E 2000;61:747.
[17] Watson JD, Crick FHC. Molecular structure of nucleic acids: a structure for deoxyribose nucleic acid. Nature 1953;171:737–8.
[18] Yoon B, Luedtke W, Barnett RN, Gao J, Desireddy A, Conn BE, Bigioni T, Landman U. Hydrogen-bonded structure and mechanical chiral response of a silver nanoparticle superlattice. Nat Mater 2014;13:807.
[19] Zheng, B., Xu, J., acceptedin press. Mechanical logic switches based on DNA-inspired acoustic metamaterials with ultrabroad low-frequency bandgaps. J Phys D
[20] Zhu R, Liu XN, Hu GK, Sun CT, Huang GL. A chiral elastic metamaterial beam for broadband vibration suppression. J Sound Vibr 2014;333:2759–73.